Slip of a liquid crystal droplet rotator in viscous fluids

Journal:	*Soft Matter*
Manuscript ID	SM-ART-08-2023-001028.R2
Article Type:	Paper
Date Submitted by the Author:	20-Nov-2023
Complete List of Authors:	Saito, Keita; Kyushu University Faculty of Sciences Graduate School of Sciences, Department of Physics Kimura, Yasuyuki; Kyushu University Faculty of Sciences Graduate School of Sciences, Department of Physics

SCHOLARONE™
Manuscripts

ARTICLE

Slip of a liquid crystal droplet rotator in viscous fluids

Keita Saito and Yasuyuki Kimura

Microscale flow plays an important role in several areas, including microbiological systems and microfluidic devices. These systems are often placed in viscous or complex fluids such as polymer solutions. Understanding microscale flow in viscous fluids will lead to a further development of microfluidic devices and elucidation of the collective motion of microorganisms. We studied the microscale flow induced by the optically driven rotation of a nematic liquid crystal (NLC) droplet in an aqueous glycerol solution. The rotation of the droplets was controlled using circularly polarized optical tweezers. In water, the induced flow agrees well with the theoretical flow assuming a solid rotating particle and a no-slip boundary condition. However, the induced flow velocity deviated from the theoretical value as the viscosity of the glycerol solution increased. This deviation was mainly due to slip on the droplet surface. As an application of the NLC rotator, the viscosity of the solutions and the hydrodynamic interactions between the two rotating particles were measured.

1. Introduction

Microscale flow plays an important role in various biological phenomena[1,2] and for particle separation in microfluidic devices.[3] For example, induced flow due to the rotation of bacterial flagella leads to a turbulence-like collective motion characteristic of bacteria.[2] A particle moving in a linear microfluidic channel is subjected to a force perpendicular to the direction of movement because of the difference in the flow velocity at the top and bottom of the particle. This force depends on the particle size; therefore, particles can be separated based on their sizes.[4] Analyzing and handling microscale flows is useful for understanding the collective motion of microorganisms and for developing cell-separation techniques. These systems are often placed in viscous or viscoelastic fluids such as bacteria in polymer solutions[5] or cells in the blood[6]. Therefore, elucidating the flow field of viscous fluids is important for understanding the behavior of microparticles in a real environment.

Optical tweezers are powerful tools for investigating microscale flows because they enable noncontact and non-destructive control of the positions of micro-objects and microscale flow.[7] Birefringent objects can be rotated by transferring the angular momentum of the light.[8] Therefore, circularly polarized light can be used to rotate birefringent objects and induce local flow fields at arbitrary positions.[9] Nematic liquid crystal (NLC) droplets are typical birefringent objects, and their rotation can be induced by circularly polarized optical tweezers.[10–13]

The rotational mechanism of NLC droplets depends on its inner structure.[13] The Inner structure of an NLC droplet varies with the size and boundary conditions of molecules on the droplet surface.[14,15] When the molecular alignment at the droplet surface is tangential, the inner structure of the droplet is bipolar, LC molecules are aligned along the surface, and there are two-point defects at the poles of the droplet.[15] For a bipolar NLC droplet, the main rotation mechanism is the waveplate effect, which has high energy efficiency.[13] The advantages of using an NLC droplet are the ease of droplet fabrication and the ability to control droplet size at the microscale.[16] Therefore, bipolar NLC droplets are appropriate for controlling microscale flows.

In this study, we investigated the flow field induced by the rotation of an NLC droplet by varying the viscosity of the surrounding solution to understand the effect of viscosity on rotation. For this purpose, the rotational frequency of the droplet and the flow velocity around the droplet were simultaneously measured using circularly polarized optical tweezers. The experimental results were discussed by comparing the rotation frequency with the magnitude of the flow velocity. We constructed a micro-viscometer using an optically trapped rotating droplet. Subsequently, hydrodynamic interaction between two rotating droplets was studied using holographic optical tweezers (HOT).[17]

2. Materials and methods

2.1 Materials

E7 (a mixture of 51 wt% 5CB (TCI), 25 wt% 7CB (Sigma-Aldrich), 16 wt% 80CB (TCI), and 8 wt% 5CT (TCI)) was used as the NLC. A mixture of E7 and ultrapure water was stirred using a vortex mixer to produce E7 droplets. The diameters of the droplets ranged from 4 to 12 μm, and the inner structure of the

Department of Physics, Kyushu University, Motooka 744, Fukuoka 819-0395, Japan;
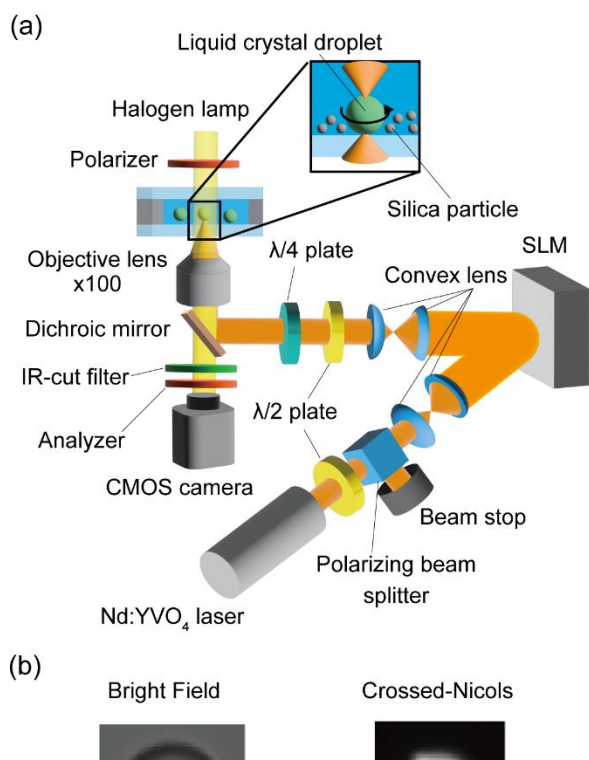E-mail: kimura@phys.kyushu-u.ac.jp

ARTICLE

(a)

(b)

Fig. 1 Experimental system. (a) Holographic optical tweezers and schematic of the sample cell. The small silica particles were added to NLC droplet dispersion for PIV measurement. (b) Microscope images of an NLC droplet under bright field (left) and crossed-Nicols polarizers (right).

droplets was bipolar.

Solid birefringent particles were prepared by mixing E7 and 15 wt% RM257 (Sigma-Aldrich, photopolymerizable monomer) with toluene.[16] After stirring the mixture (E7 and RM257) with a magnetic stirrer for 3 h, toluene was evaporated. The droplets were prepared in the same manner as E7 droplets. They were irradiated with ultraviolet light for 30 min for solidification via photopolymerization.

The droplets dispersed in water or aqueous glycerol solutions were sealed in a glass cell that was approximately 85 μm thick.

2.2 Methods

The wavefront of the laser beam (YLM-10-CP, IPG Photonics, wavelength λ: 1064 nm) was modified using a spatial light modulator (SLM, X10468-03, Hamamatsu) to control the spatial intensity pattern in the focal plane, as shown in Fig. 1(a). The reflected beam was modulated to circularly polarized light using a pair of 1/2 and 1/4 waveplates. The polarized beam was focused using a 100 × objective lens (Plan Fluor, Nikon, NA1.4). The E7 droplets were trapped approximately 10 μm above the bottom of the cell to avoid wall effects. The laser power ranged from 5.6 to 47 mW.

Images of the droplets were captured every 10 ms using a complementary metal-oxide-semiconductor (CMOS) camera (OrcaFlash 4.0, Hamamatsu, 2048 × 2048 pix²) attached to an inverted optical microscope (Eclipse Ti, Nikon). The rotation frequency of the droplet was estimated from the temporal

change in the image intensity captured by crossed Nicols polarizers.[13] Images captured under the bright field were used for the particle image velocimetry (PIV) analysis.

Silica particles (Sicastar-greenF, Micromod) with 0.15 wt% and a diameter of 500 nm were used as tracer particles to visualize the flow field. Because the silica particles sedimented at the bottom, rotating droplets were set at the bottom of the cell. The captured images were analyzed using the PIV lab in MATLAB to calculate the flow field.[18]

3. Results and discussion

3.1 Induced flow field in viscous fluids

A bipolar NLC droplet receives optical torque Γ by circularly polarized beam via waveplate effect, $\Gamma \propto E^2(1 - \cos\Delta)$, where E is the amplitude of electric field of incident beam and Δ is the retardance described by $\Delta = 4\pi\Delta na/\lambda$ (Δn: the birefringence, a: radius of the droplet).[11,13] Angular frequency ω is determined by balance between optical torque Γ and viscous resistance from a surrounding fluid[19],

$$\Gamma = 8\pi\eta a^3\omega, \tag{1}$$

where η is the viscosity of the surrounding fluid and no-slip boundary condition is assumed. The flow fields around a droplet were measured by PIV. It was difficult to measure the flow field near the droplet due to fringe pattern at the vicinity of the surface (An image of the fringe pattern is shown in the supplementary information). The flow field induced by an NLC droplet in a 60 wt% aqueous glycerol solution was compared with that in water, as shown in Figs. 2(a) and 2(b). The flow fields were similar, except for the magnitude of the flow velocity. The tangential component of induced flow velocity v_θ at distance r from the center of the rotating particle is expressed as[19]

$$v_\theta = \frac{a^3}{r^2}\omega. \tag{2}$$

Eqn (2) assumes a solid spherical particle and no-slip boundary condition. We took the radial average of v_θ and compared the measured v_θ with the theoretical value estimated using Eqn (2), as shown in Figs. 2(c) and 2(d). In water, the measured dependence of v_θ on r is in good agreement with the theoretical one estimated by Eqn (2) shown by a solid line in Fig. 2(c). This confirms that the droplet behaved as a solid particle. Because the viscosity of E7 was several tens of times higher than that of water,[20] the droplet in water could be regarded as a solid. In contrast, in the 60 wt% aqueous glycerol solution, the measured values of v_θ were smaller than the theoretical values according to Eqn (2) (solid line in Fig. 2(d)).

First, the effect of changes in the refractive index of the solutions on Γ was examined. The refractive index of the solution depends on the mass concentration of glycerol C_m. The refractive indices of water (C_m = 0 wt%) and the aqueous
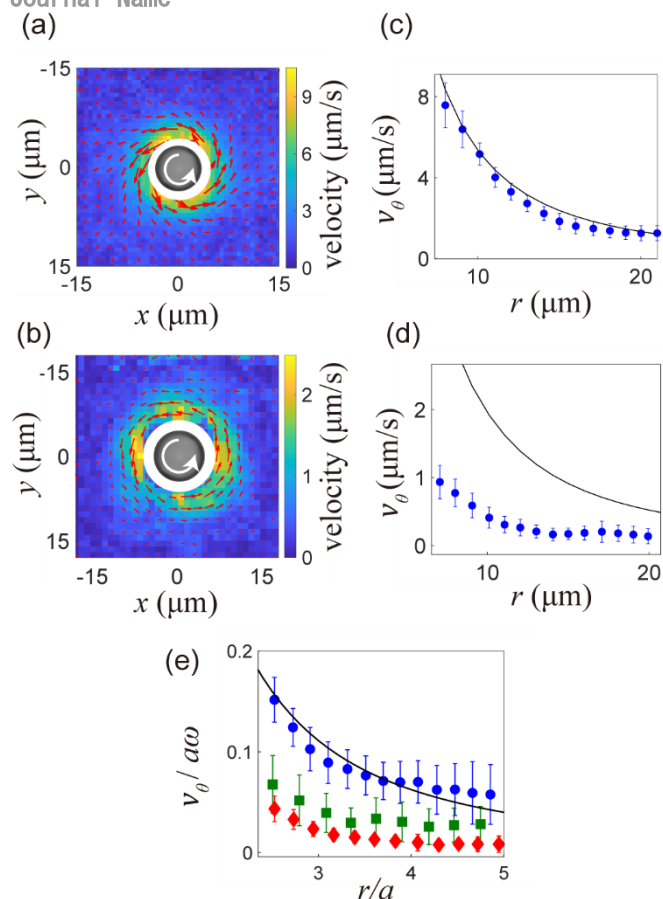
ARTICLE

Fig. 2 Flow field induced by a rotating NLC droplet. (a) Flow fields in water. (b) Flow fields in a 60 wt% aqueous glycerol solution. The laser power used was 28.2 mW. The white circle represents the area where flow velocity cannot be correctly measured by PIV, and microscopic image of an NLC droplet was placed at the center of the white circles. The white arrow indicates the direction of rotation. Radius a in (a) is 3.4 µm and (b) is 4.5 µm. The red arrows represent local velocity vectors. (c, d) Variation in the azimuthal component of induced flow velocity v_θ with the distance r from the droplet center in water (c) and in the glycerol solution (d). The solid line represents theoretical values determined by Eqn (2) (e) Variation in the scaled azimuthal component of induced flow velocity $v_\theta/a\omega$ with the scaled distance r/a from the droplet center: a droplet in water (filled blue circles) corresponding to (a), a droplet in the 60wt% aqueous glycerol solution (filled red diamonds) corresponding to (b), an optically cured particle (a = 3.6µm) in 60wt% aqueous glycerol solution (filled green squares) and theoretical values determined by Eqn (2) (solid line).

glycerol solution (C_m = 60 wt%) are 1.33 and 1.42, respectively.[21] The amplitude of the electrical field inside droplet E_d is expressed by the Fresnel equation under normal incidence as follows:

$$E_d = \frac{2n_1}{n_1 + 2n_2} E_{in}, \quad (3)$$

where E_{in} is the incident electric field and n_1 and n_2 are the refractive indices of the solution and liquid crystal, respectively (n_2 = 1.50 for E7[22]). The variation in n_1 changes the amplitude of the electric field. Because the optical torque Γ is proportional to the square of the electric field E_d^2,[11] Γ at C_m = 60 wt% increases by 6 % compared with Γ at C_m = 0 wt% with a fixed laser power. The change in Γ expected from the variation of the refractive index is relatively small. Therefore,

this was ruled out as the major reason for the discrepancy between the theoretical (Eqn (2)) and experimental values of Γ.

Next, we considered the wall effect on the tracer particles because the particles were settled down near the cell bottom.[23] Effective viscosity η_{eff} is expected to increase due to the particle-wall interaction. We estimated η_{eff} by observing Brownian motion of the particle near the bottom (detail discussion is presented in the supplementary information). At C_m = 60 wt%, the calculated η_{eff} is 9.8 mPa·s and this is larger than literature one in bulk η_0 (8.8 mPa·s).[24] The velocity of the particle near the bottom is reduced by about 11% due to the increase in effective viscosity. The measured velocity from PIV was corrected by multiplying η_{eff}/η_0 by the measured velocity to remove the influence the velocity reduction due to the wall effect. In addition, the solution viscosity relative to the droplet increased because the droplet was also closer to the bottom. Experimental observations show that the viscosity at the bottom is approximately 1.1 times the bulk viscosity η_0.[13] However, the decrease in v_θ relative to the theoretical value estimated by Eqn (2) at C_m = 60 wt% cannot be explained by wall effect alone.

We consider the origin of the difference between the results in water and those in the aqueous glycerol solution to be a violation of the assumptions of a solid particle and the no-slip boundary condition. Possible origins are fluidization inside the droplet and slippage at the surface of the droplet. Due to fluidity of LC, the disagreement between the direction of LC director and flow velocity inside the LC has been reported in a rotating cholesteric LC pillar.[25] To verify these possibilities, we used optically cured solid particles (a mixture of E7 and 15 wt% RM257) that showed no internal fluidization in water.[16] We compared $v_\theta/a\omega$ for the droplet and a cured particle as shown in Fig. 2(e) because $v_\theta/a\omega$ can be scaled by r/a as in Eqn (2). The average ratio of v_θ for the droplet to the estimated one by Eqn (2) was 0.21, which can be attributed to both slip and fluidization inside the droplet. Conversely, the ratio of the cured particle was 0.4. In this case, only the slip contributed to this decrease. The viscous resistance of a droplet is $\frac{2\eta_s+3\eta_d}{3(\eta_s+\eta_d)}$ times smaller than that of a solid particle where η_d and η_s are the viscosities of the liquids inside and outside the droplet, respectively.[26] Even in C_m = 60 wt%, the factor, $\frac{2\eta_s+3\eta_d}{3(\eta_s+\eta_d)}$, is 0.94 where $\eta_d = 40$ mPa·s and $\eta_s = 8.8$ mPa·s.[20,24] This decrease (0.06) due to fluidization is relatively small to the whole reduction of the flow velocity. We considered that the remaining difference between the droplet and the cured one was attributed to changes in slip condition arising from the polymerization. In both cases, the slip at the surface appeared to have a dominant influence on the decrease in the induced flow velocity. The tangential component of the induced flow
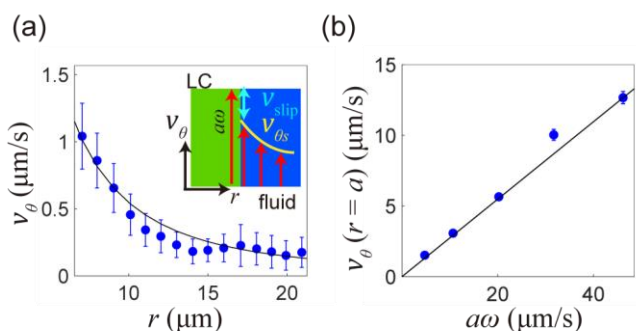
ARTICLE

Fig. 3 Flow field induced by an NLC rotator (radius a = 3.4 μm) in a 60 wt% aqueous glycerol solution. (a) Variation in the tangential component of the flow field v_θ with the distance r from the center of the droplet with a 28.2 mW laser power. The solid line represents the best-fitted curve of Eqn (4) with β = 3.50 × 10³ N·s/m³. The inset represents a schematic of a velocity profile under the slip boundary condition. (b) Variation in the flow velocity at the droplet surface $v_\theta(a)$ with $a\omega$ (a: fixed). The laser power used ranged from 9.4 mW to 47 mW. The solid line is the theoretical value determined using Eqn (4) with the same β as in (a).

velocity $v_{\theta s}$ under the slip boundary condition is written as,[27-29]

$$v_{\theta s} = \frac{\beta a}{\beta a + 3\eta} \frac{a^3}{r^2} \omega, \qquad (4)$$

where β is the slip coefficient and the particle-wall interaction is not considered. The corrected measured data was used by removing the influence of the particle-wall interaction. The measured dependence of corrected v_θ on r in the glycerol solution at C_m = 60 wt% can be fitted using Eqn (4) with fixed ω and the fitting parameter β, as shown in Fig. 3(a). The optimal value of β is 3.50×10³ N·s/m³ and the corresponding slip velocity is 14.6 μm/s. In this study, slip velocity v_{slip} is the difference between surface velocity of the droplet and flow velocity at the surface, $v_{\text{slip}} = a\omega - v_{\theta s}(a)$, as schematically shown in the inset of Fig. 3(a). This value is comparable in magnitude to the slip velocity reported for microchannels (from 30 to 50 μm/s[30]). The variation of v_θ at the droplet surface with $a\omega$ was also measured by changing the power of the incident beam, as shown in Fig. 3(b). The experimental results agree well with the theoretical equation $v_{\theta s}(a) = \frac{\beta a}{\beta a + 3\eta} a\omega$, which is a modified version of Eqn (4) using the same β as in Fig. 3(a). This confirmed that the slip effect was dominant. In a cholesteric LC droplet, the disagreement between the calculated flow velocity by the droplet rotation and the measured one is also observed.[31] The slippage at the droplet surface has been cited as one of the possible origins of this disagreement. Slip phenomena are widely observed at the interface between the polymer solution and solid surface,[32] and the initial shear stress at which slip occurs is normally as large as 10⁵ Pa.[33] However, at the liquid–liquid interface, the initial shear stress is smaller than that at the solid–liquid interface, with a value of approximately 4 Pa.[34] In our experiment, the shear stress acting on the droplet $\eta \left.\frac{\partial v_{\theta s}}{\partial r}\right|_{r=a}$ was approximately 0.02 Pa where η = 9.8 mPa·s, β was 3.50×10³
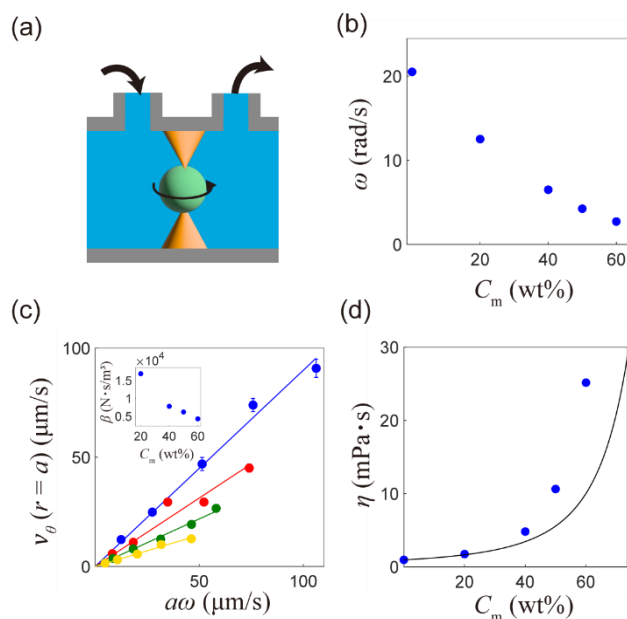

Fig. 4 Micro-viscometer utilizing an NLC droplet in aqueous glycerol solutions. (a) Schematic of the micro-viscometer. The surrounding solution is exchanged via holes at the top. The black arrow represents the direction of solution flow during solution exchange. (b) Variation in rotation frequency ω with C_m. Radius a of a droplet was 5.2 μm and the laser power used was 18.8 mW. (c) Variation in the flow velocity at the droplet surface $v_\theta(a)$ with $a\omega$ in 20 wt% (filled blue circles, a = 2.5 μm), 40 wt% (filled red circles, a = 2.8 μm), 50 wt% (filled green circles, a = 3.8 μm) and 60 wt% (filled yellow circles, a = 3.4 μm) glycerol solutions. The laser power used ranged from 9.4 mW to 47 mW. The solid line represents the linearly fitted line (blue: 20 wt%, red: 40 wt%, green: 50 wt% and yellow: 60 wt%). The inset represents the variation in the slip coefficient β with C_m. (d) Variation in viscosity η of the glycerol solutions with the mass concentration C_m measured by our micro-viscometer. The solid line represents literature values.[24]

N·s/m³, a = 3.4 μm and ω = 6.0 rad/s, which is two orders of magnitude lower than the above value. Although the origin of the slip is unclear in this study, it may be related to the alignment of the LC molecules. In a glycerol solution, the NLC molecules align along the surface because glycerol induces planer anchoring.[35] The surface roughness with planer anchoring is smoother than that with homeotropic anchoring.[36] The slip easily occurs for a smoother surface.[37] We assume that this is also applicable to an LC droplet, and the planer anchoring promotes slippage at the interface. Further, intermolecular interactions at the interface also affects the slip.[38] Since the adhesive force between glycerol and 5CB (main component of used LC) in the nematic phase due to hydrogen bond is weaker than that between water and 5CB, slip at the glycerol-5CB interface is more likely to occur.[39] Adding glycerol could reduce the adhesion force between the droplet surface and the surrounding fluid and promotes sliding.

3.2 Application of NLC droplet as a micro-viscometer

For the application of the rotating droplet, we used a droplet as a micro-viscometer. In our micro-viscometer, a single rotating droplet was captured with optical tweezers while varying the glycerol mass concentration C_m in a laboratory-made flow device, as schematically shown in Fig. 4(a). Rotational angular

velocity ω of the same droplet at the same laser power was measured for each C_m. Because the viscosity of the solution increased with increasing C_m, the measured ω decreased with increasing C_m, as shown in Fig. 4(b). In water, the optical torque Γ_W was estimated using Eqn (1) with a literature value of η, Γ_W = 0.804 pN·μm. In the aqueous glycerol solutions, the boundary condition changed to slip boundary condition. The viscous torque in the slip boundary condition Γ_{slip} is $\frac{\beta a}{\beta a + 3\eta}$ times the viscous torque in the no-slip boundary condition, $\Gamma_{\mathrm{slip}} = 8\pi\eta\omega a^3 \frac{\beta a}{\beta a + 3\eta}$.[29] In slip condition, $\eta = \frac{\Gamma}{8\pi\omega a^3}\left(\frac{\beta a}{\beta a + 3\eta}\right)^{-1}$. To estimate of the factor $\frac{\beta a}{\beta a + 3\eta}$, the variation of v_θ at the droplet surface with $a\omega$ was measured by changing the power of the incident beam in several C_m, as shown in Fig. 4(c). Since the variation of v_θ was described by modified Eqn (4) $v_{\theta s}(a) = \frac{\beta a}{\beta a + 3\eta} a\omega$, we can obtain $\frac{\beta a}{\beta a + 3\eta}$ from the slope of the best-fitted line to data. We also considered the increase of Γ due to changes in the refractive index n using Eqn (3). At low η, the estimated η agreed with the literature value[24], as shown in Fig. 4(d). Because an NLC droplet behaves as a solid one because the viscosity of the NLC is much higher than that of solutions, fluidization inside the droplet is negligible at low η. However, at high η, a discrepancy becomes apparent. With the above correction method, the difference between the rotation speed and flow velocity is attributed only to slippage at the surface. η may have been overestimated because the effects of slip and fluidization were not properly separated at this stage.

3.3 Measurement of hydrodynamic interaction

As another application of LC droplets, we studied the hydrodynamic interactions between two rotating droplets in the same direction. We measured the dependence of rotation frequency ω on the interparticle distance l by controlling trap patterns with an SLM under crossed-Nicols polarizers, as shown in the inset of Fig. 5(a). Water and a 70 wt% aqueous glycerol solution were prepared as the surrounding media. In water, when the droplets were close together (l < 7 μm), both ω for the left and the right droplet decreased as the droplets approached each other, as shown in Fig. 5(a). As the optical torque varies slightly with the trapping position, ω gradually decreases with l even if the droplets were sufficiently separated (l > 12 μm). The rotation frequency ω_{ith} of the i-th droplet, considering the hydrodynamic interaction with the Ronte-Prager approximation is written as[27,28]

$$\omega_{ith} = \frac{\Gamma_i}{8\pi\eta a_i^3} - \frac{\Gamma_j}{16\pi\eta l^3}, \tag{5}$$

where i and j are the indices of particle ($i \neq j$). We measured ω for each droplet in the single-particle system and estimated Γ using Eqn (1). The measured values are in good agreement with the calculated values by Eqn (5), as indicated by the solid line in Fig. 5(a). We replaced the surrounding medium with a glycerol solution and measured the dependence of ω on l in the same manner as described above. We compared the
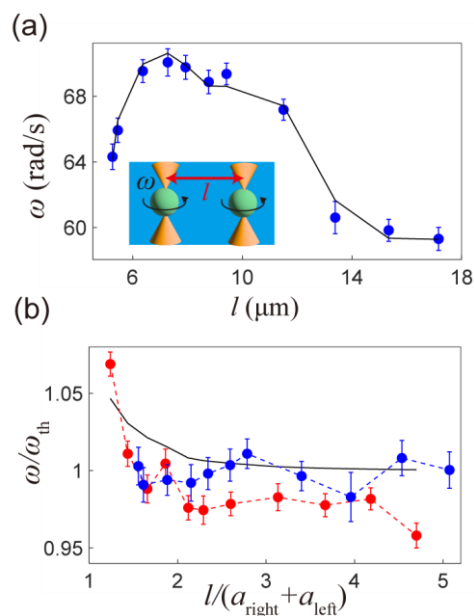

Fig. 5 Rotating frequencies of two particles placed at distance l. (a) Variation of rotation frequency ω of the left particle with l in water with 5.6 mW laser power. The solid line represents the calculated values using Eqn (6) under the no-slip boundary condition. The inset represents a schematic of two particles rotating in a sample cell. (b) Ratio of the measured values ω to the theoretical ones ω_{th} estimated by Eqn (5) in water (blue dots) and a 70 wt% aqueous glycerol solution (red dots). The solid line represents the calculated values using Eqn (6) under the slip boundary condition. The horizontal axis is normalized by contact distance $a_{\mathrm{right}} + a_{\mathrm{left}}$, where a_{right} is the radius of the right droplet and a_{left} is that of the left one.

measured values with the calculated values for the water and glycerol solutions, as shown in Fig. 5 (b). Ratios ω/ω_{ith} were almost close to one in water, which is consistent with the results shown in Fig. 5(a). Ratios ω/ω_{ith} were also almost close to one in the glycerol solution, except for the nearest-neighbor distance ($\frac{l}{a_{\mathrm{right}} + a_{\mathrm{left}}}$ = 1.2). When l is small, the second term on the right side of Eqn (6) becomes large, and Γ_j becomes significant for ω. In the case of the slip being significant, slip reduces viscous torque Γ_j. The viscous torque in the slip boundary condition Γ_{slip} is $\frac{\beta a}{\beta a + 3\eta}$ times larger than that in the no-slip boundary condition, $\Gamma_{\mathrm{slip}} = 8\pi\eta\omega a^3 \frac{\beta a}{\beta a + 3\eta}$.[29] The value of β in C_m = 70 wt% was estimated by linear extrapolation with three data points in the inset of Fig. 4(c), β = 2.1×10^3 N·s/m^3. We calculated ω derived from Eqn (5) with Γ_{slip}, as shown in the solid line of Fig. 5(b). The calculated ω also slightly larger than unity when l is small, and this supports the reduction of hydrodynamic interaction due to the slip.

4. Conclusions

The rotational motion of an NLC droplet in aqueous glycerol solutions was studied using circularly polarized optical tweezers. In water, the flow field induced by the rotation of the droplet was in good agreement with the theoretical field

ARTICLE

according to Eqn (2), assuming solid–particle and no-slip boundary conditions. However, the induced flow velocity in the glycerol solution was lower than the theoretical value estimated by Eqn (2). This suggests that the assumptions of the solid particle and no-slip boundary conditions may have been violated. Using the optically cured particles, we tested whether the fluidization effect or slip at the droplet surface was dominant. The results indicated that the slip at the droplet surface was dominant in the reduction of the induced flow field. The degree of slip increased with increasing solution viscosity.

We have shown examples of application for the NLC droplet rather than the cured particle because NLC droplets are very easy to fabricate. As a first application of the NLC droplet, we used a droplet as a micro-viscometer. For a medium with low η, the estimated values were in good agreement with the literature values. Conversely, the difference from the literature values became larger as η increased. Accurate estimation of the fluidization effect and the slip effect seems important to estimate η at high viscosity. In practice, solid rotating particles, such as vaterite crystals, are normally utilized to study the local viscosity.[40,41] As another application, the hydrodynamic interaction between rotating particles was measured by monitoring ω of each particle. In water, the measured ω agreed well with the theoretical values calculated using the Ronte-Prager approximation. In the glycerol solution, the measured value was larger than the theoretical value estimated by Eqn (5) owing to slip when the interparticle distance was small.

The origin of the slippage is unresolved at this stage. We considered the alignment of LC molecules at the droplet surface was related to a reduction in the flow field. The NLC molecules on the glycerol surface aligned along the droplet surface (homogenous alignment), and this alignment appeared to be relevant to slip.

This study provides insights into microscale flow induced by rotating droplets in viscous fluids. This knowledge will lead to the further development of opto-microfluidic devices in viscous fluids.

Author Contributions

K.S. and Y.K. designed this study; constructed the experimental system; acquired, analyzed, and interpreted the data; and prepared the draft of this paper.

Conflicts of interest

There are no conflicts to declare.

Acknowledgements

Notes and references

1. E. Lauga and T. R. Powers, *Rep. Prog. Phys.*, 2009, **72**, 096601.
2. E. Lauga, *Annu. Rev. Fluid Mech.*, 2016, **48**, 105–130.
3. P. Sajeesh and A. K. Sen, *Microfluid. Nanofluidics.*, 2014, **17**, 1–52.
4. J.-S. Park and H.-I. Jung, *Anal. Chem.*, 2009, **81**, 8280–8288.
5. J. Elgeti, R. G. Winkler and G. Gompper, *Rep. Prog. Phys.*, 2015, **78**, 056601.
6. L. Lanotte, J. Mauer, S. Mendez, D. A. Fedosov, J.-M. Fromen-tal, V. Claveria, F. Nicoud, G. Gompper and M. Abkarian, *Proc. Natl. Acad. Sci. U.S.A.*, 2016, **113**, 13289–13294.
7. M. Padgett and R. Di Leonardo, *Lab Chip*, 2011, **11**, 1196–1205.
8. M. E. Friese, T. A. Nieminen, N. R. Heckenberg and H. Rubinsztein-Dunlop, *Nature*, 1998, **394**, 348–350.
9. R. Di Leonardo, J. Leach, H. Mushfique, J. Cooper, G. Ruocco and M. Padgett, *Phys. Rev. Lett.*, 2006, **96**, 134502.
10. S. Juodkazis, S. Matsuo, N. Murazawa, I. Hasegawa and H. Misawa, *Appl. Phys. Lett.*, 2003, **82**, 4657–4659.
11. T. A. Wood, H. F. Gleeson, M. R. Dickinson and A. J. Wright, *Appl. Phys. Lett.*, 2004, **84**, 4292–4294.
12. E. Brasselet and S. Juodkazis, *J. Nonlinear Opt. Phys. Mater.*, 2009, **18**, 167–194.
13. K. Saito and Y. Kimura, *Sci. Rep.*, 2022, **12**, 16623.
14. J. K. Gupta, S. Sivakumar, F. Caruso and N. L. Abbott, *Angew. Chem. Int. Ed.*, 2009, **48**, 1652–1655
15. P. S. Drzaic, *Liquid crystal dispersions*, World Scientific, 1995.
16. X. Wang, E. Bukusoglu and N. L. Abbott, *Chem. Mater.*, 2017, **29**, 53–61.
17. J. E. Curtis, B. A. Koss and D. G. Grier, *Opt. Commun.*, 2002, **207**, 169–175.
18. W. Thielicke and R. Sonntag, *J. Open Res. Softw.*, 2021, **9**, 1.
19. L. D. Landau and E. M. Lifshitz, *Fluid Mechanics,* Butterworth-Heinemann, 1959.
20. W. Martienssen and H. Warlimont, *Springer Handbook of Condensed Matter and Materials Data*, Springer, 2005.
21. I. Pala Rosas, J. L. Contreras, J. Salmones, C. Tapia, B. Zeifert, J. Navarrete, T. Vázquez and D. C. García, *Catalysts*, 2017, **7**, 73.
22. V. Tkachenko, G. Abbate, A. Marino, F. Vita, M. Giocondo, A. Mazzulla, F. Ciuchi and LD Stefano, Mol. Cryst. Liq. Cryst., 2006, **454**, 263-271.
23. J. Happel and H. Brenner, *Low Reynolds number hydrodynamics: with special applications to particulate media*, Springer, 1981.

Please do not adjust margins

ARTICLE

24. N.-S. Cheng, *Ind. Eng. Chem. Res.*, 2008, **47**, 3285–3288.

25. J. Yoshioka. and F. Araoka, *Sci. Rep.*, 2020, **10**, 17226.

26. E. Guyon, J. P. Hulin, L. Petit and C. D. Mitescu, *Physical Hydrodynamics*, Oxford, 2015.

27. J. Rotne and S. Prager, *J. Chem. Phys.*, 1969, **50**, 4831–4837.

28. H. Yamakawa, *J. Chem. Phys.*, 1970, **53**, 436–443.

29. A. Basset, *A treatise on Hydrodynamics*, Dover, 1961.

30. P. Joseph, C. Cottin-Bizonne, J.-M. Benoit, C. Ybert, C. Journet, P. Tabeling and L. Bocquet, *Phys. Rev. Lett.*, 2006, **97**, 156104.

31. K. Nishiyama, S. Bono, Y. Maruyama and Y. Tabe, *J. Phys. Soc. Jpn.*, 2019, **88**, 063601.

32. R. Tuinier and T. Taniguchi, *J. Phys. Condens. Matter*, 2004, **17**, L9.

33. S. G. Hatzikiriakos, *Prog. Polym. Sci.*, 2012, **37**, 624–643.

34. J. Koplik and J. R. Banavar, *Phys. Rev. Lett.*, 2006, **96**, 044505.

35. P. Poulin, H. Stark, T. Lubensky and D. Weitz, *Science*, 1997, **275**, 1770–1773.

36. R. Zibaei, M. S. Zakerhamidi, S. Korram and A. Ranjkesh, *J. Mater. Chem. C*, 2021, **9**, 14908-14915.

37. S. Granick, Y. Zhu and H. Lee, *Nat. Mater.*, 2003, **2**, 221-227.

38. B. Weber, Y. Nagata, S. Ketzetzi, F. Tang, W. J. Smit, H. J. Bakker, E. H. G. Backus, M. Bonn, and D. Bonn, *J. Phys. Chem. Lett.*, 2018, **9**, 2838–2842.

39. Z. Wang, Q. Xu, L. Wang, L. Heng and L. Jiang, *J. Mater. Chem. A*, 2019, **7**, 18510–18518.

40. A. I. Bishop, T. A. Nieminen, N. R. Heckenberg and H. Rubinsztein-Dunlop, *Phys. Rev. Lett.*, 2004, **92**, 198104.

41. S. Zhang, L. J. Gibson, A. B. Stilgoe, T. A. Nieminen and H. Rubinsztein-Dunlop, *J. Biophotonics*, 2019, **12**, e201900022.

Please do not adjust margins